Simulating the mid-Holocene, Last Interglacial and mid-Pliocene climate with EC-Earth3-LR

Qiong Zhang[1], Qiang Li[1], Qiang Zhang[1], Ellen Berntell[1], Josefine Axelsson[1], Jie Chen[1,2], Zixuan Han[1], Wesley de Nooijer[1], Zhengyao Lu[3], Klaus Wyser[4], Shuting Yang[5]

[1]Department of Physical Geography, Stockholm University, Stockholm, 10691, Sweden
[2]College of Earth and Environmental Sciences, Lanzhou University, Lanzhou, 730000, China
[3]Department of Physical Geography and Ecosystem Science, Lund University, Lund, 22100, Sweden
[4]Rossby Centre, Swedish Metrological and Hydrological Institute, Norrköping, 60176, Sweden
[5]Danish Meteorological Institute, Copenhagen, 2100, Denmark

Correspondence to: Qiong Zhang (qiong.zhang@natgeo.su.se)

Abstract. Paleoclimate modelling has long been regarded as a strong out-of-sample test-bed of the climate models that are used for the projection of future climate changes. For the first time, the EC-Earth model contributes to the Paleoclimate Model Intercomparison Project (PMIP) phase 4, which is part of the current sixth phase of the Coupled Model Intercomparison Project (CMIP6). Here, we document the model setup for PMIP4 experiments with EC-Earth3-LR and present the results on the large-scale features from the completed production simulations for the three past warm periods (mid-Holocene, Last Interglacial, and mid-Pliocene). Using the pre-industrial climate as a reference state, we show the changes in global temperature, large scale Hadley circulation and Walker circulation, polar warming and global monsoons, as well as the climate variability modes (ENSO, PDO, AMO). The EC-Earth3-LR simulates reasonable climate responses during past warm periods as shown in the other PMIP4-CMIP6 model ensemble. The systematic comparison of these climate changes in three past warm periods in an individual model demonstrates the ability of the model to capture the climate response under different climate forcings, providing potential implications for confidence in future projections with EC-Earth model.

1 Introduction

The Coupled Model Intercomparison Project phase 6 (CMIP6) provides the scientific base for the sixth IPCC report assessment report (IPCC AR6). CMIP6 includes experiments for the past climate regimes, coordinated by the Paleoclimate Modelling Intercomparison Project phase 4 (PMIP4). The aim of PMIP4 is to understand the response of the climate system to the climate forcings that are very different from present and historical periods. The existing climate reconstructions based on physical, chemical, or biological records from natural archives provide evidence on past climate changes, which can be used to test the ability of state-of-the-art climate models performing PMIP experiments to simulate those climate changes. This information can be used to assess the credibility of climate projections for future climate change.

The PMIP4 experiments are designed for simulations of five different climates to contribute to the objectives on climate change in the CMIP6: the millennium prior to the industrial epoch (name in CMIP6 database: *past1000*); the mid-Holocene, 6000 years ago (the *midHolocene*); the Last Glacial Maximum, 21 000 years ago (the *lgm*); the Last Interglacial, 127 000 years ago (the *lig127k*); and the mid-Pliocene Warm Period, 3.264–3.025 million years ago (the midPliocene-eoi400, hereafter is referred to as the *midPliocene*). The scientific motivation for the

choice of these periods, as well as the protocols of the numerical experiments are presented in Kageyama et al. (2018).

40

All the participating modelling groups are required to follow the PMIP4 protocols as described in Kageyama et al. (2018). The detailed justification of the experimental protocols for each period are described separately in several PMIP4 experiment design papers: Otto-Bliesner et al. (2017) for the *midHolocene* and *lig127k* experiments, Kageyama et al. (2017) for the *lgm*, Jungclaus et al. (2017) for the *past1000*, and Haywood et al.

45 (2016) for the *midPliocene* experiment. These past periods are characterized by changes in boundary conditions such as greenhouse gas concentrations (e.g. the *midPliocene*), orbital parameters (e.g. the *midHolocene* and the *lig127k*), extensive ice sheet extent (the *lgm*), and volcanic and solar activities different from the current or historical ones (the *past1000*). The large-scale features from the PMIP4 multi-model ensemble have been evaluated for respective PMIP4 experiment for the *midHolocene* (Brierley et al., 2020), *lig127k* (Otto-Bliesner et

50 al., 2020), *lgm* (Kageyama et al., 2020) and *midPliocene* (Haywood et al., 2020).

EC-Earth3-LR is one of the models that contribute to PMIP4. For an individual climate model, the PMIP4 experiments contribution provides an opportunity to test the climate response to different forcing and gives an overview of the past climate change in one model system. The Last Glacial Maximum climate is much colder

55 than present day and requires a long spin-up process to reach the quasi-equilibrium. The *lgm* simulation using EC-Earth3-LR is still in running and the boundary condition implementation and results will be evaluated in a stand-alone paper. For the last millennium simulation (the *past1000*), it is crucial to include the evolution of the land use, which requires the inclusion of a dynamical vegetation coupling. We used another model configuration EC-Earth3-veg-LR with a coupled dynamical vegetation model for the *past1000* experiment, therefore this

60 experiment will be documented in a stand-alone paper as well.

In the present paper, we document the experiments setup and the model performance for the pre-industrial, the mid-Holocene, the Last interglacial and the mid-Pliocene with EC-Earth3-LR. The chosen three time-slice PMIP4 experiments are the past warm periods, and although the climate responses are determined by the different

65 forcings, these past warm periods are often used as future analogue from different aspects. We expect that a systematic comparison across different past climates in one individual model can improve our understanding on the global warming through different forcings and provide a more solid scientific base to evaluate the future climate projections.

70 In the following presentation we use the *piControl*, the *midHolocene*, the *lig127k* and the *midPliocene* to refer the official PMIP-CMIP6 experiment names (except for the midPliocene-eoi400 that we use a short version *midPliocene*). In the illustrations we use abbreviations PI, MH, LIG and MPlio to refer the four experiments.

2 The EC-Earth model description

2.1 EC-Earth model components and the configuration

75   The EC-Earth is a fully coupled earth system model that integrates a number of state-of-art components in the climate system including atmosphere, ocean, sea ice, land and biosphere. It is developed by the European consortium of research institutions and widely used in various studies on climate change (Hazeleger et al., 2010; Hazeleger et al., 2012). The CMIP6 model version of EC-Earth3.3 is based on the ECMWF integrated forecasting system (IFS) cy36r4, the ocean model NEMO3.6 coupled to the sea ice model LIM3 with five sea ice categories,

80   and the dynamic vegetation model LPJ-Guess. EC-Earth3 also includes the atmospheric chemistry component TM5 and the ocean biogeochemistry component PISCES. The EC-Earth3 model contributes to CMIP6 in several configurations by using different resolutions or including different components. A detailed description of the EC-Earth3 and its contribution to CMIP6 is documented in Döscher et al. (2020).

85   The PMIP4 experiments require long spin-up and equilibrium simulations which are computationally demanding. We thus use model configurations without atmospheric chemistry and ocean biogeochemistry at low resolution. For the *piControl*, the *midHolocene*, the *lig127k*, and the *midPliocene*, we have used the EC-Earth3-LR, which is a configuration of EC-Earth3 with only atmosphere, ocean and sea ice components at Low-Resolution (LR). Here the atmosphere model IFS and land model H-TESSEL have a TL159 horizontal resolution (around 125 km) and

90   the atmosphere has 62 vertical layers with the model top at 5 hPa. The horizontal resolution for the ocean model NEMO3.6 and sea ice model LIM3 is about 1° (the so-called ORCA1 configuration), and the ocean has 75 vertical levels. Despite using the lowest resolution among the EC-Earth3 CMIP6 MIPs configuration, EC-Earth3-LR has a relatively high resolution compared to the other PMIP4 models (Brierley et al., 2020).

2.2 Implemented physics that needed for paleo-simulations

95   Two important physical processes, i.e. orbital forcing and physics over the ice-sheet, that are crucial for paleoclimate simulations, are implemented in the EC-Earth3. Below, we describe the implementation of these two physics in the EC-Earth3.

2.2.1 Orbital forcing

Previous versions of the EC-Earth treated the orbital forcing as constants for the present-day climate in IFS, by

100   following the recommendations of the International Astronomical Union. These formulas are not valid for dates too far away from the 1st January 2000 (if more than one century). To facilitate the paleoclimate simulations, the orbital forcing is calculated in the atmosphere component IFS using the method of (Berger, 1978). The new orbital parameterization use Julian calendar to calculate the cosine of the solar zenith angle according to the model time. The Julian calendar has two types of year: a normal year of 365 days and a leap year of 366 days. To follow the

105   Gregorian calendar used in IFS, which contains leap year, the orbital parameter calculation follows a simple cycle of three normal years and one leap year, giving an average year that is 365.25 days long. The annual and diurnal cycle of solar insolation are thus represented with a repeatable solar year of exactly 365.25 days and with a mean solar day of exactly 24 hours, respectively. The year must fall within the range of 1950 ± 106. In the EC-Earth model run script, there are two ways to set the orbital forcing, either to change the three orbital parameters to

110   known values corresponding to the certain year (defaults are for 1950), or to specify a number for the year. To specify the year, for AD year the exact year number applies, e.g. for 1850 we set "*ifs_orb_iyear = 1850*". For the year before AD, the distance to reference year 1950 is given, for example, the mid-Holocene, which is 6000 years before present day, can be specified as -4950 (obtained from -6000+1950). For the equilibrium simulations, the orbital forcing is fixed for each year, and we therefore set "*ifs_orb_mode = fixed*".

115   **2.2.2 Albedo parameterization of snow on ice-sheet**

Concerning the ice-sheet mass balance, the original land surface scheme HTESSEL used in IFS does not treat ice sheets explicitly. The surface scheme assumes the ice-sheet as 10 meters of perennial snow, and it is in thermal contact with the underlying soil. The albedo and snow density are fixed at 0.8 and 300 kg m^3, respectively. The fixed, high snow albedo value over ice sheet makes it difficult for the snow melting due to lack of albedo feedback.

120   This process becomes crucial especially for past periods with large ice-sheet extents, such as LGM. Therefore, we introduce a new albedo parameterization of snow on ice-sheet, where snow melting become possible and occurs often. This varying snow albedo scheme is also active for the configuration of EC-Earth3 coupled with interactive ice sheet model for Greenland ice sheet, i.e. EC-Earth3-GrIS (Döscher et al, 2020). A comparison among different albedo parameterizations on Greenland ice-sheet is summarised in Helsen et al. (2017) using EC-

125   Earth3. The time-varying snow albedo better represents the ice/snow-albedo feedback and is beneficial for both cold and warm climates. From EC-Earth3, the snow is not allowed to accumulate for more than 9 meters of water equivalent. All excessive snow falls on the ice-sheet is immediately redistributed into the ocean and will not accumulate on ice sheet. This treatment has an advantage of energy and mass conserving, and the calving ice cools the ocean along the coast which helps to reduce the warm bias in the Southern Ocean.

130

The above mentioned two physics are included in the CMIP6 version EC-Earth3, with on and off options. For the PMIP4 experiments, we have applied these new physical implementations. However, other CMIP6 experiments e.g. future projections have not applied these new implementations.

3 The experiment design and setup with EC-Earth3-LR

135   **3.1 PMIP4-CMIP6 protocols on climate forcings and boundary conditions**

We follow the PMIP4 protocol and implement the climate forcings and boundary conditions for each PMIP4 experiment as documented in (Kageyama et al., 2018). The climate forcings implemented in the four experiment are listed in Table 1.

140   **Table 1**. PMIP4-CMIP6 protocols on forcings and boundary conditions.

	piControl	*midHolocene*	*lig127k*	*midPliocene*
Eccentricity	0.016764	0.018682	0.039378	Same as *piControl*
Obliquity (degrees)	23.549	24.105	24.040	Same as *piControl*

Perihelion - 180	100.33	0.87	275.41	Same as *piControl*
CO_2 (ppm)	284.3	264.4	275	400
CH_4 (ppb)	808.2	597	685	Same as *piControl*
N_2O (ppb)	273.0	262	255	Same as *piControl*
Topography & land-sea mask	Modern	Same as *piControl*	Same as *piControl*	Enhanced topography as in Haywood et al. (2016)
Ice sheets	Modern	Same as *piControl*	Same as *piControl*	As in Haywood et al. (2016)
Vegetation	CMIP DECK *piControl*	Same as *piControl*	Same as *piControl*	Salzmann et al. (2008)

For all the four experiments, the solar constant is 1360.747 W/m², which is fixed for *piControl* at the mean value for the first two solar cycles of the historical period 1850-1871 (Erying et al., 2016). The Vernal equinox is fixed at noon on March 21. Aerosols including dust and volcanic are set as the *piControl* value. Datasets for *midPliocene*

145   from the PRISM4 reconstructions are downloaded from PlioMIP2 website:
(https://geology.er.usgs.gov/egpsc/prism /7.2 _pliomip2_data.html).

**3.2 Boundary condition implementation for the *midHolocene* and *lig127k***

In the PMIP4 Tier 1 for the *midHolocene* and the *lig127k* experiments, the changes in boundary conditions are

150   orbital parameters and greenhouse gas concentrations (Table 1). As described earlier, the setting for orbital forcing and greenhouse gas in the EC-Earth3-LR is straightforward. In the model run script, we set "*Orb_year = - 4950*" for the *midHolocene* and "*Orb_year = - 125050*" for the *lig127k*, the computed orbital parameters are exactly the same as those listed in Table 1.

155   The changes in orbital parameters, in particular the higher obliquity in the *midHolocene* and *lig127k*, lead to large changes in seasonal and latitudinal distribution of the insolation, with stronger changes in the *lig127k* than in the *midHolocene* (Fig. 1). The global changes in annual mean insolation is negligible. The Northern Hemisphere (NH) receives 20 W m⁻² more insolation during boreal summer June-August in the *midHolocene* and 48 W m⁻² in May-July in *lig127k*. While in boreal wintertime it receives 14 W m⁻² less in February-March in the *midHolocene*

160   and 36 W m⁻² less during October-November in the *lig127k*. The maximum changes occur in the high latitudes, i.e. the Arctic region (60 - 90° N) receives 31 W m⁻² more in July in the *midHolocene* and 70 W m⁻² more in June in *lig127k*. The Southern Hemisphere (SH) receives 23 W m⁻² and 56 W m⁻² more in September and October in the *midHolocene* and *lig127k* respectively. These large insolation changes in high latitudes cause polar amplification (Sect. 4.4). The positive insolation anomalies in summer months lead to strong land-sea contrast

165   and enhance the monsoons (Sect. 4.5).

The greenhouse gas concentration is provided by CMIP6, for the *piControl* the values are taken from the values at the year 1850 in the historical forcing files. An easy way for other PMIP4 periods is simply to create a new file by changing those values in year 1850 to the values specified in Table 1.

170
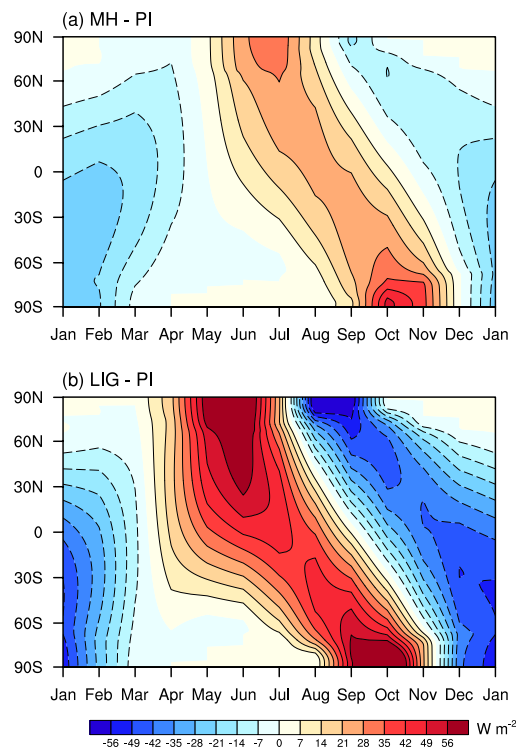
Figure 1. Changes in the latitudinal and seasonal distribution of insolation (W m^{-2}) as compared to the *piControl*, (a) the *midHolocene*, (b) the *lig127k*. The modern calendar is used, with vernal equinox on 21 March at noon.

175   **3.3 Boundary condition implementation for the *midPliocene***
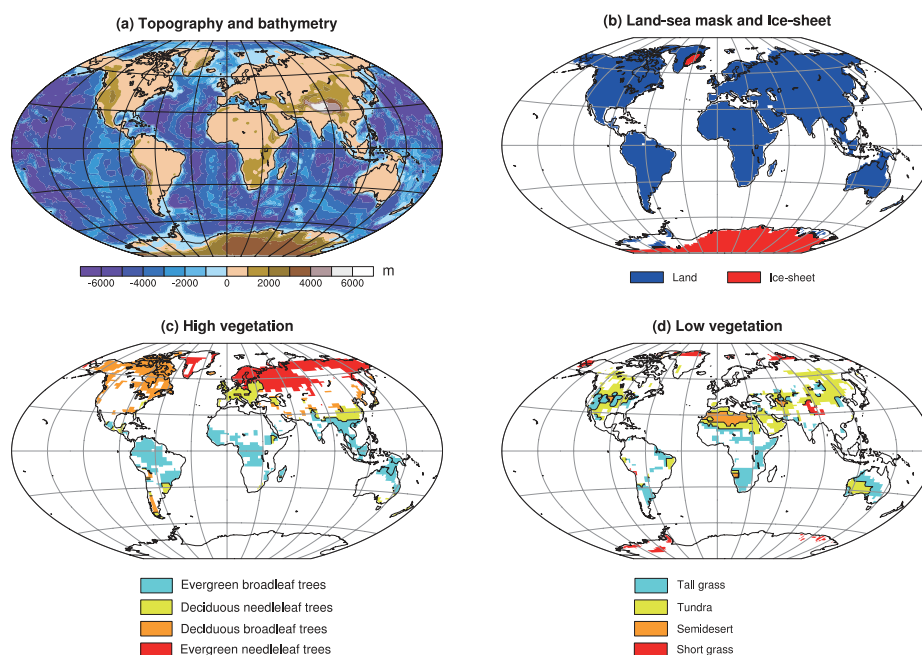
Figure 2. Prescribed boundary conditions for mid-Pliocene adapted to EC-Earth resolution. (a) topography and bathymetry (unit, metre), (b) land-sea mask and ice sheet, (c) high-vegetation and (d) low vegetation.

180   In the PlioMIP2 protocol, the mid-Pliocene period is centred at an interglacial peak (marine isotope stage KM5c) at around 3.025 Ma, which has similar orbital forcing to present-day. Since the differences between using the 3.025 Ma orbit and the present-day orbit are very small (de Boer et al., 2017), therefore the orbital parameters are kept the same as in *piControl*. For the PlioMIP2 Tier 1 experiment, the CO_2 concentration in the atmosphere is set at 400 ppm. CH_4 and N_2O are specified as identical to those in the *piControl* experiment. We have used the

185   enhanced boundary condition according to PRISM4 reconstruction (Dowsett et al., 2016), which considers change in dynamic topography associated with mantle flow and glacial isostatic adjustment due to Piacenzian ice loading. The changes in topography includes the closure of the Bering Strait and the straits through the Canadian Arctic Archipelago. The topography, land-sea-mask, bathymetry and ice sheet from PRISM4 are implemented to the EC-Earth3-LR atmosphere and ocean horizontal grid (Fig. 2). The global distributions of soil and biome are

190   modified to match the *midPliocene* land-sea mask and ice-sheet reconstruction. Due to the change of land-sea mask, there are emergence of new land areas, and rivers are routed to the nearest ocean point.

Following the PlioMIP2 protocol, we prescribe the vegetation from PRISM3 reconstruction data (Salzmann et al., 2008). The reconstructed vegetation is a 9-type mega-biome map classified after (Harrison and Prentice, 2003).

195   In the EC-Earth3 land model HTESSEL, the vegetation type classification is based on the Biosphere-Atmosphere Transfer Scheme (BATS) model (Yang and Dickinson, 1996) which contains 20 biome classifications. For each

grid point, it is characterised by a maximum of two dominant vegetation types, high vegetation and low vegetation, and their area fractions. The sum of the high and low vegetation coverage is always between 0 and 1. Therefore a translation from mega biome to HTESSEL classification is performed. We first re-gridded the mega-biome

200   reconstruction data to the EC-Earth3 TL159 horizontal grid. Then the translation is done grid by grid with the correspondence between the two biomes (Table. 2). The final vegetation types are shown as four types of low vegetation and four types of high vegetation in HTESSEL (Fig. 2). Due to the present translation scheme, each grid will have only one vegetation type, representing either a high or low vegetation. See Table. 2 for details.

205   **Table 2**. The translation/correspondence between reconstructed mega-biome to EC-Earth HTESSEL vegetation type. H/L refer to the distinction between high (H) and low (L) vegetation.

Reconstructed Mega biome	HTESSEL vegetation type (H/L)
Tropical Forest	Evergreen broadleaf trees (H)
Warm-Temperate Forest	Evergreen needleleaf trees (H)
Savanna/dry woodland	Tall grass (L)
Grassland/dry shrub	Short grass (L)
Desert	Semidesert (L)
Temperate forest	Deciduous broadleaf trees (H)
Boreal forest	Deciduous needleleaf trees (H)
Tundra	Tundra (L)
Dry tundra	Tundra (L)

3.4 Initial conditions, spin-up and production

210   A *piControl* spin-up with EC-Earth3-LR configuration is carried out during the model tunning process and contains for minor changes in the simulation process. The initial conditions for the *piControl*, the *midHolocene* and *lig127k* are taken from the end of the *piControl* spin-up phase (which ran for approximately 1000 years). Our *piControl* differs from the version of spin-up *piControl* by applying the new implementation of orbital forcing and land-ice physics, therefore it takes around another 200 years of spin-up phase for this *piControl* simulation to

215   reach the equilibrium state. The criteria for an equilibrium state are measured by the global mean surface temperature trend < +/- 0.05 °C per century and a stable Atlantic meridional overturning circulation (AMOC) (Kageyama et al., 2018). Due to the changed boundary conditions, the *midHolocene* and *lig127k* simulations reach the equilibrium state after about 200 years spin-up. The *midPliocene* experiment starts from the initial condition of a Levitus ocean state, and a spin-up of 1400 years is performed until it reaches the equilibrium state. The change

220   in land-sea mask in *midPliocene* requires proper initial fields for the changed grid-box, these fields are all modified by the model and are expected to reach equilibrium with the given boundary conditions.
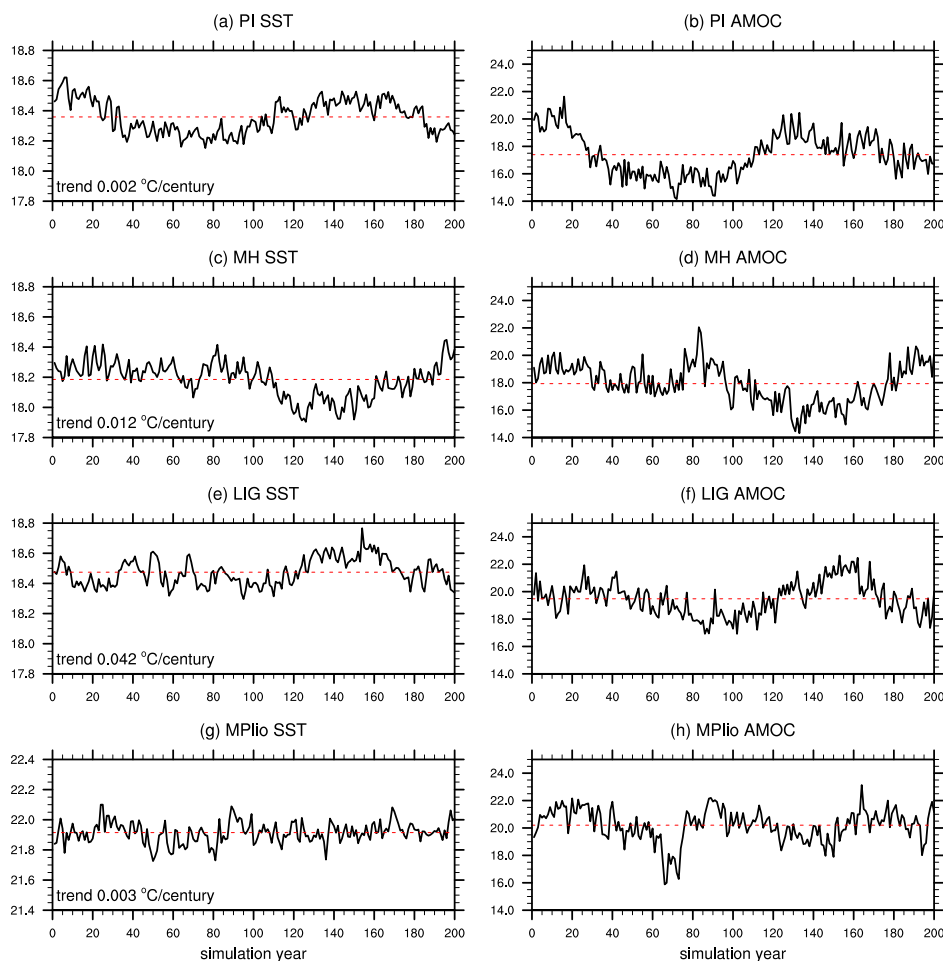
Figure 3. Evolution of annual mean globally averaged SST (°C, left panel) and annual mean maximum AMOC (Sv, right panel) in spin-up period for (a, b) the *piControl*, (c, d) the *midHolocene*, (e, f) the *lig127k* and (g, h) the *midPliocene* simulation. The 200 years mean is indicated with a red dash line.

The time evolution of the global mean SST and the maximum AMOC are presented in Fig. 3 for the four simulations. To be comparable we show 200 years spin-up period for all the four experiments. The trends in global mean sea surface temperature in the four spin-up have met the criteria of equilibrium. In the EC-Earth3-LR simulations, the maximum AMOC mostly appears at 25° N latitude, and occasionally shifts northward to 45° N. AMOC is about 17.5 Sv *piContro* simulation and becomes stronger in the *midHolocene, lig127k* and *midPliocene* simulations. The multidecadal variability is apparent in both AMOC and SST in the *piControl,* the *midHolocene* and *lig127k* simulations. The *midPliocene* is the warmest period and show less low frequency variability.

In the supplement we have shown the time evolution during the 200 years spin-up period for more variables. The energy balance at the top of the atmosphere and at the surface are stable in all the simulations (a-b in Fig. S1-S4).

9

Though for an equilibrium state we expect a closure of energy in the atmosphere-ocean system, all our simulations show approximately - 0.5 W m^{-2} imbalance (TOA energy minus surface). To reduce this energy imbalance is one

240   major target in model tunning process under the pre-industrial climate condition and the tunned parameters are not allowed to change in any other past or future scenarios according to the CMIP6 protocol. The 0.5 W m^{-2} energy leak in EC-Earth3-LR is in the range of pre-industrial control simulations in 25 CMIP5 climate models (Hobbs et al., 2016). One reason may be due to the insufficient spin-up as the deep ocean temperature and salinity have shown larger trend (Fig. S1-S4) than that of the surface temperature (Fig. 3). The deep ocean temperature

245   has exhibited an increasing trend in all the four simulations. The deep ocean salinity shows a decreasing trend in *piControl* and *midHolocene* but an increasing trend in *lig127K* and *midPliocene*. Considering the climates are warmer in the latter two conditions, both sea-ice melting in the polar regions and enhanced oceanic evaporation can influence the surface salinity in different ways. More diagnostics in ocean dynamics are needed to understand these deep ocean features in different climate scenarios. No apparent trend is seen in the sea-ice extent in the

250   Arctic and Antarctic (Fig. S1-S4). The Arctic sea-ice shows the similar low frequency variability as seen in AMOC (right panel in Fig. 3), indicating the association between the Arctic sea ice and AMOC. The dramatic overall sea-ice melting is seen in *midPlocene*, in both Arctic and Antarctic. In the other three experiments, the Antarctic sea-ice extent remains similar to that of *piControl*. These climate mean features in sea-ice in spin-up period remains in the production simulation, which is performed from the end of each spin-up. We present the

255   large-scale features from 200 years production simulations in section 4.

3.5 Post-processing of the model output for PMIP4-CMIP6

Following the format of the CMOR tables (Climate Model Output Rewriter, an output format in conformance with all the CMIP standards), we use a software ece2cmor3 package for the model output post-processing. Ece2cmor3 is a python package developed by the EC-Earth community for converting the EC-Earth3 model

260   output to the CMIP6 compliant format. It uses Climate Data Operators (CDO) (Schulzweida, 2019) and the CMOR library bindings to select variables and vertical levels, perform time-averaging (or take daily extrema), interpolate the spectral and grid-point atmospheric fields to a regular Gaussian grid and compute derived 305 variables by arithmetic combination of the original model fields. The ece2cmor3 package uses the PCMDI CMOR-library for the production of netCDF files with the appropriate format and metadata. All the data presented

265   in this paper are publicly available at CMIP6 database at https://esgf-node.llnl.gov/projects/cmip6/.

It is worth noting that a particular caution should be paid for downloading the *piControl* data from ESGF data nodes. There are several *piControl* by the EC-Earth3 model available in the CMIP6 database. It is appropriate to select the one with the model name EC-Earth3-LR as the reference for the other PMIP4 experiments. The other

270   *PiControl* experiments by EC-Earth3 differ in the model configuration or model resolution.

4. Climate responses in the *midHolocene*, *lig127k* and *midPliocene* simulations

Here we present the changes in the large-scale features of the three past warm climates simulated by the EC-Earth3-LR, i.e., the two interglacial simulations *midHolocene* and *lig127k*, as well as the high CO$_2$ featured *midPliocene,* with the comparison to the reference simulation *piControl*.

275   **4.1 Global mean temperature anomalies**

The global annual mean values for climate anomalies from the three experiments with respect to the *piControl*
are summarised in Table 3. The global mean temperature from the *midHolocene* shows a slightly cooling, placing
the simulation towards the upper end of the PMIP4 *midHolocene* ensemble (Brierley et al., 2020). The global
mean precipitation anomaly is mild in the *midHolocene*, with about 5-7 % more precipitation than in *piControl*

280 over the land during the boreal summer and autumn, following the enhanced Northern Hemisphere monsoon (Sect.
4.5). The larger changes in orbital forcing in the *lig127k* results in 0.4 °C warming globally, and this warming is
amplified over the land and in the Arctic. In the *lig127k,* the land precipitation increased 16 % in boreal summer,
indicating a stronger monsoon than in the *midHolocene*. The *midPliocene* shows a significant global warming
reaching 4.8 °C, which is among one of the warmest simulations with highest Arctic amplification in the PlioMIP2

285 ensemble (Haywood et al., 2020; de Nooijer et al., 2020). The precipitation is increased more than 10 % globally
and the land precipitation increased more than 20 % in boreal summer and autumn season in the *midPliocene*.

Table 3. Global mean temperature and precipitation anomalies with respect to the *piControl*.

Experiment	Season	Surface air temperature anomalies					Precipitation anomalies mm/day (percent change)		
		Global	Land	Sea	60°N-90°N (75°N-90°N)	60°S-90°S (75°S-90°S)	Global	Land	Sea
midHolocene	ANN	-0.1	0	-0.1	1.3 (1.4)	0.1 (-0.1)	0 (0)	0.04 (1.7)	-0.02 (-0.6)
	DJF	-0.2	-0.4	-0.1	1.1 (1.1)	-0.08 (-0.54)	0.03 (1)	-0.03 (-1.2)	0.07 (2.2)
	MAM	-0.7	-0.9	-0.5	0.2 (0.1)	-0.42 (-0.82)	-0.02 (-0.7)	-0.07 (-3.1)	0 (0)
	JJA	0.2	0.5	0	1.6 (1.9)	-0.02 (0)	-0.02 (-0.7)	0.12 (5.0)	-0.10 (-3.2)
	SON	0.5	0.7	0.4	2.1 (2.7)	0.72 (1.04)	0.02 (0.7)	0.15 (6.6)	-0.06 (-2.0)
lig127k	ANN	0.4	0.7	0.2	3.6 (4.3)	-0.14 (-0.15)	0.03 (1.0)	0.10 (4.3)	-0.01 (0.3)
	DJF	-0.6	-0.8	-0.5	2.8 (3.4)	-0.99 (-1.70)	0.03 (1.0)	-0.17 (-7.2)	0.14 (4.4)
	MAM	-0.3	0.1	-0.5	2.9 (3.1)	-0.82 (-1.12)	-0.06 (-2.1)	0.06 (2.6)	-0.13 (4.2)
	JJA	1.7	3.0	1.0	5.0 (4.8)	0.03 (0.15)	0.03 (1.0)	0.38 (15.9)	-0.17 (5.4)
	SON	0.8	0.6	0.9	3.6 (5.8)	1.23 (2.10)	0.12 (4.3)	0.12 (5.2)	0.12 (3.9)
midPliocene	ANN	4.8	6.3	4.0	11.6 (13.1)	8.28 (10.4)	0.31 (11.0)	0.45 (19.4)	0.23 (7.4)
	DJF	4.6	5.9	3.9	10.6 (12.6)	6.91 (8.33)	0.27 (9.4)	0.37 (15.7)	0.21 (6.7)
	MAM	4.4	6.1	3.8	10.8 (10.3)	8.45 (11.61)	0.29 (10.4)	0.41 (18.1)	0.21 (6.7)
	JJA	4.9	6.5	4.0	11.0 (9.5)	9.71 (11.85)	0.35 (12.3)	0.49 (20.6)	0.26 (8.3)
	SON	5.13	6.70	4.2	14.1 (20.0)	8.05 (9.86)	0.33 (11.9)	0.51 (22.4)	0.23 (7.5)

4.2 Response in annual mean temperature

We first show a comparison between the annual mean temperature in *piControl* with early century (1901-1930)
290 mean in ERA20C reanalysis data (Fig. 4a). The EC-Earth3-LR tends to overestimate the temperature in high
latitudes, with cold biases in NH and warm biases in SH. This is a fairly robust feature in most of the global
climate models in particular prominent in EC-Earth model and the cause it attributed to the simulated sea ice
(Koenigk et al., 2013; Chapman and Walsh, 2007). In the following analysis we compare the anomalies in the
three paleoclimate experiments with respect to the *piControl*, any changes in the temperature reflect the responses
295 to the external forcing.
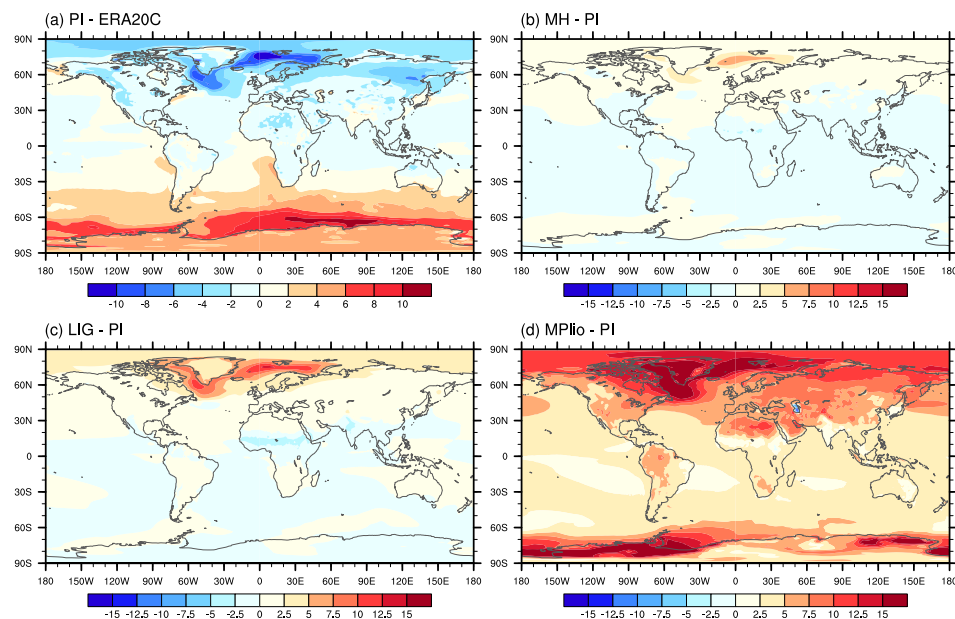
Figure 4. Mean annual temperature (°C) in (a) difference between the *piControl* and ERA20C (1901-1930 mean),
and the anomaly in the (b) the *midHolocene*, (c) the *lig127k* and (d) the *midPliocene* from the *piControl*.

300 The orbital forcing during the two interglacial periods is characterized by the redistribution of the insolation over
the globe in different seasons (Fig. 1). This does not affect too much of the global energy balance, therefore the
climate changes in global mean are insignificant (Table 3). The spatial patterns of mean annual temperature show
warming in the Arctic region in the two interglacial periods relative to the pre-industrial, with a larger magnitude
in the *lig127k* than in the *midHolocene* (Fig. 4b and Fig. 4c). The warming in southern high latitudes shown in
305 the PMIP4 *midHolocene* ensemble (Brierley et al., 2020) is not apparent in EC-Earth3-LR simulation. The
simulated *midPliocene* warming is much stronger than those of the two interglacial periods, dominated by the
strong Arctic amplification in EC-Earth3-LR (de Nooijer et al., 2020). In the *midPliocene* the strong warming
amplification appears in both polar regions (Fig. 4d), which contrasts the weak warming in some parts in the
southern high latitudes in the *midHolocene* and *lig127K* (Fig. 4b and Fig. 4c). The seasonal features of the

310   temperature response in the polar regions are discussed more in detail in Sect. 4.4. In all the three warm periods, the response in annual mean temperature is stronger over the land than over the ocean (Fig. 4 and Table 3), which is a common feature in most PMIP4-CMIP6 simulations (Brierley et al., 2020; Otto-Bliesner et al., 2020; Haywood et al., 2020). These notable changes in polar amplification and land-sea contrast modulate the temperature gradients and lead to changes in the large-scale circulation (Sect. 4.3) and global monsoons (Sect.

315   4.5).

4.3 Response in Hadley circulation and Walker circulation
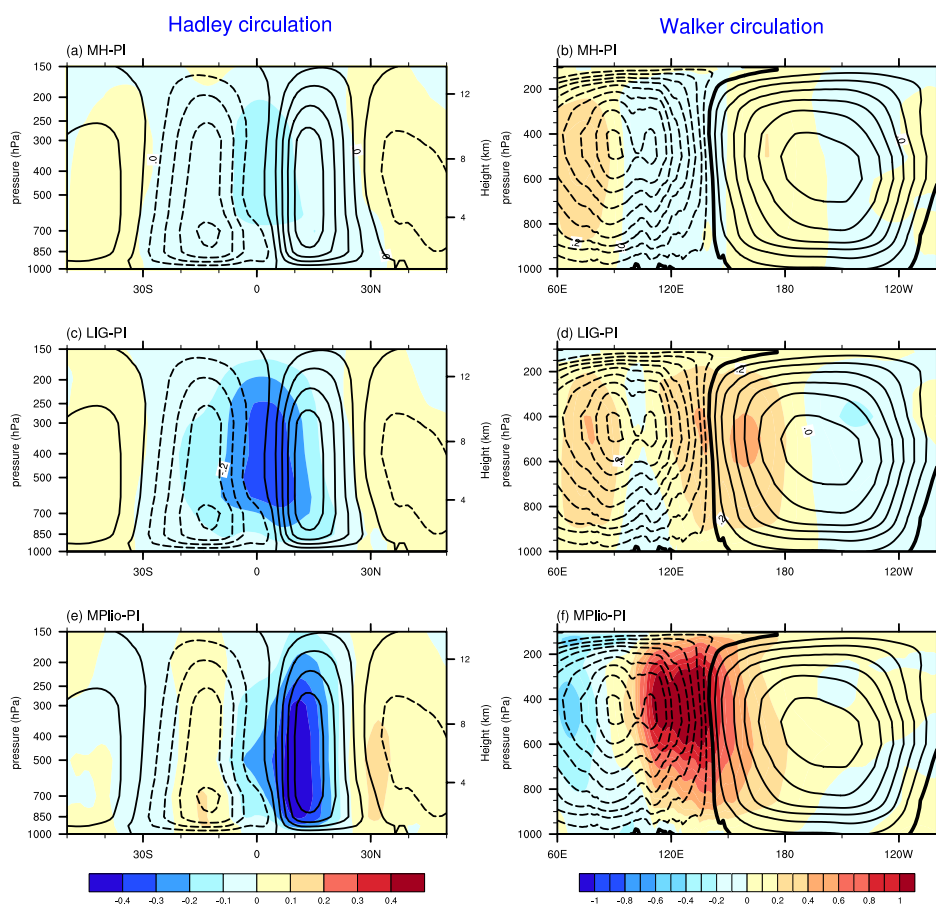
Figure 5. The changes in annual mean Hadley circulation (represented by zonal-mean meridional mass stream function in the left panel) and Walker circulation (represented by zonal mass stream function averaged between

320   10º S~10º N over Indo-Pacific region 60º E-150º W in the right panel). The shadings indicate the changes in (a, b) the *midHolocene*, (c, d) the *lig127k* and (e, f) the *midPliocene* respect to *piControl*. The contours represent the climatology from the *piControl* simulation (solid contours indicate positive value and dashed contours indicate negative value). Units: 10^{10} kg s^{-1}.

325   The changes in global temperature pattern, shown above, could induce large atmospheric circulation anomalies,
       i.e. in the Hadley circulation and Walker circulation. Previous studies have demonstrated that the meridional
       surface air temperature gradient between low latitude and mid-to-high latitude determine the changes in Hadley
       circulation (Corvec and Fletcher, 2017; Burls and Fedorov, 2017). Indeed, the weakening of the Hadley circulation
       seen in the NH in the three experiments (Fig. 5a, 5c and 5e) are corresponding to the decreased temperature
330   gradient between tropics and mid-to-high latitude (Fig. 4b-d). However, the thermal contrast is less pronounced
       in the Southern Hemisphere in the *midHolocene* and the *lig127k* simulations. The two simulations even show
       slight cooling in the SH compared to the tropics (Fig. 4b and 4c), result in a slightly stronger meridional
       temperature gradient, and induce weaker Hadley circulation (Fig. 5c). In the *lig127k* and *midPliocene* simulations
       we observe a poleward widening of Hadley circulation in both Hemisphere. This widening is less obvious in the
335   *midHolocene* simulation.

       The Walker circulation in *piControl* is characterised as ascending in the maritime continent and western Pacific
       and descending in the eastern Pacific (contours in Fig. 5b, 5d and 5e), which is consistent with previous studies
       (Peixoto and Oort, 1992; Kamae et al., 2011; Bayr et al., 2014). Compared to the *piControl*, all three warm period
340   simulations show strong ascending over the tropical western Pacific, indicating a strengthening and westward
       shift of the Pacific Walker circulation cell (Fig. 5b, 5d and 5f). There is more westward shift in the *lig127k* and
       midPliocene compared to the *midHolocene* simulation, corresponding to less ascending over the maritime
       continent. The increasing magnitude of shift from *piControl* to *midHolocene*, *lig127k* and *midPliocene* can be
   associated with reduced ENSO variability (Sec 4.6).

345   **4.4 Climate responses in polar region**

       The response of the poles to the different boundary conditions is of particular interest as the largest temperature
       anomalies are observed here (Fig. 4), which are known to associate with strong feedbacks at the poles such as ice-
       albedo and carbon cycle feedbacks (Masson-Delmotte et al., 2013). The amplification of global temperature
       anomalies in the Arctic is a near-universal feature of historical simulations in response to the increased greenhouse
350   gas and is also observed in the instrumental record (Serreze and Barry, 2011). Similar amplification of global
       temperature anomalies is not observed in the Antarctic, which may be attributed to the rapid removal of surface
       heat in the Southern Ocean, which, in turn, limits the ability of climate feedbacks to amplify the warming (Stroeve
       et al., 2007). Arctic amplification is prominent in the EC-Earth3-LR *midPliocene* simulation, with Arctic (60-90°
       N) temperature anomalies exceeding global temperature anomalies by a factor 2.4 (Table 3). The Arctic warming
355   in the *midHolocene* and *lig127k* simulations are not as striking as in the *midPliocene*. Given that the global mean
       temperature anomalies in the *midHolocene* and *lig127k* simulations are small (Table 3), it is inappropriate to apply
       an amplification ratio as discussed in (Hind et al., 2016).

       The minimum Arctic surface air temperature (SAT) warming is expected in the summer because of increased
360   ocean heat uptake following reductions in sea ice, while maximum SAT warming is expected in the (boreal)
       autumn and winter following the release of this heat (Pithan and Mauritsen, 2014; Serreze et al., 2009; Yoshimori
       and Suzuki, 2019; Zheng et al., 2019). This expected seasonality of SAT is not present in the Arctic in the
       midHolocene and *lig127k* simulations (Fig. 6). There are peaks in Arctic SAT warming, amounting to +2.3° C

and +5.8° C in the *midHolocene* and *lig127k* simulations, respectively, in the boreal summer (Fig. 6a) due to
365   positive insolation changes (Fig. 1). Negative insolation changes during the autumn may offset some of the
expected autumn excess heat release. In the *midPliocene* simulation, Arctic SAT warming peaks in the autumn at
+15.2° C, but there is no clear summer minimum (Fig. 6a). In the Antarctic, the SAT seasonality in the two
interglacial simulations does not differ greatly from the *piControl* simulation. In the *midPliocene*, Antarctic
warming peaks in late austral winter and early spring (July-September) with maximum warming reaching +10.4°
370   C in August.
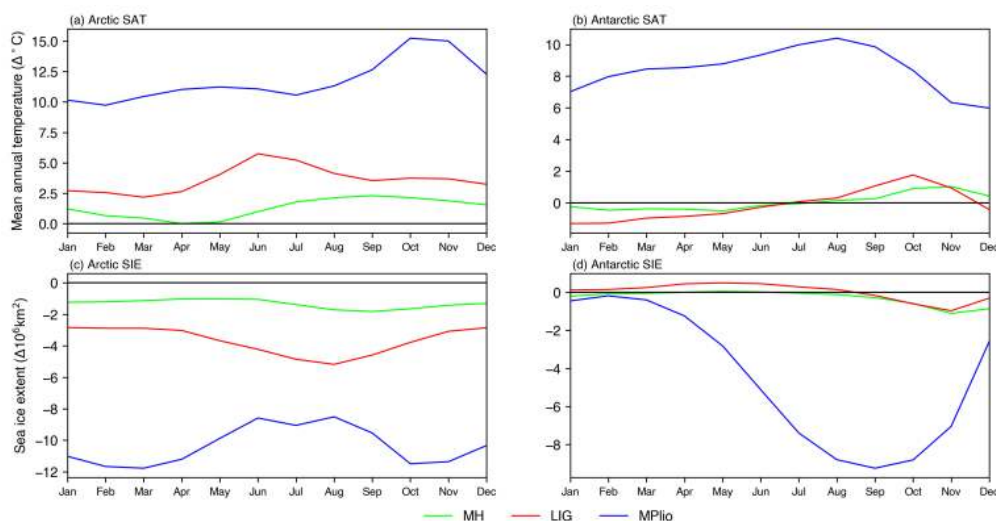
Figure 6. Seasonal changes of Arctic mean surface air temperature (a and b) and sea ice extent (c and d) in Arctic
(a and c, 60° N-90° N average), and Antarctic (b and d, 60° S-90° S average) for each simulation.

375

In comparison with the *piControl*, the simulations show significant decreases in sea ice extent (SIE) with
anomalies in the Arctic peaking at -1.8 x 10^6 km^2 in the *midHolocene*, -5.2 x 10^6 km^2 in the *lig127k*, and -11.8 x
10^6 km^2 in the *midPliocene*. SIE anomalies peak earliest in the year in the *lig127k* simulation, followed by the
midHolocene (Fig. 7c). In the *midPliocene* simulation, the Arctic experiences sea ice free conditions from August
380   to October, and anomalies peak both in the (boreal) autumn and the spring. The different timing of the SIE
anomaly peaks may be explained by a runaway sea ice-albedo feedback (Feng et al., 2019) in which early summer
reductions in SIE lead to more warming through decreased albedo and, in turn, even greater reductions in SIE.
Since the positive insolation changes in the Arctic occur earlier in the year in the *lig127k* than in the *midHolocene*,
this feedback would be triggered earlier in the year in the *lig127k*. The importance of this feedback is dependent
385   on the annual amplitude of SIE, and since this is relatively small in the *midPliocene*, results in the weakest link
between the seasonal SIE and SAT cycles. This may explain the absence of a distinct minimum in Arctic SAT
anomalies in the boreal summer in the *midPliocene* simulation. The seasonal cycle of Antarctic SIE anomalies
closely resembles the SAT cycle, and anomalies peak in September at -9.2 x 10^6 km^2 in the *midPliocene*
simulation. Anomalies are around zero throughout the year in the *midHolocene and lig127*, consistent with the
390   limited changes in SAT observed at these latitudes throughout the year.

15
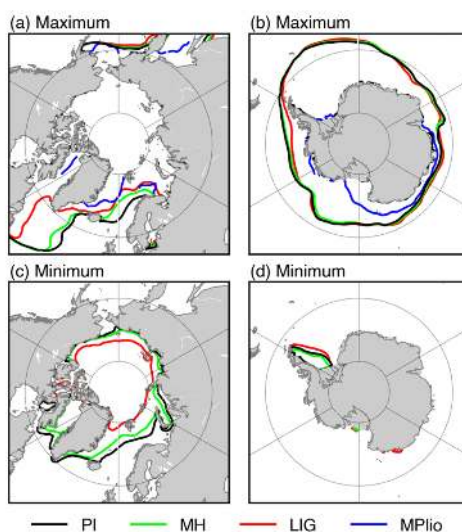
Figure 7. Sea ice edge in Arctic (a, c) and Antarctic (b, d) in the maximum (a, b) and minimum (c, d) SIE month in each simulation. Maximum sea ice extents occur in March in the Arctic, and in September in the Antarctic, while minimum sea ice extents are seen in August in the Arctic, and in February in the Antarctic.

395

The sea ice edge in the months of maximum and minimum SIE in each simulation is depicted by Fig. 7. The maximum SIE in Arctic is observed in March for each simulation (Fig. 7a). For the Arctic minimum SIE, observed in August, the sea ice edge is limited to the Greenland Sea for the *piControl* and *midHolocene* simulations in the Atlantic domain, while it does not reach farther than the Fram Strait in the *lig127k* simulation (Fig. 7c). In the

400 Antarctic, the maximum SIE is in September (Fig. 7b). Sea ice is present along most of the coast of Antarctica during September in the *midPliocene* simulation (Fig. 7b). The minimum SIE is observed in February, the sea ice edge is mainly limited to the Weddell Sea for the *piControl*, *midHolocene*, and *lig127k* simulations, while no sea ice is present in the *midPliocene* simulation (Fig. 7d).

4.5 Responses in global monsoon systems

405 We compare the global monsoon area in different simulations in Fig. 8. Here the global monsoon area is defined as the regions where the annual range precipitation exceeds 2 mm day^{-1} and the local summer precipitation exceeds 55% of the annual precipitation (Liu et al., 2009). The annual range refers to the precipitation difference between May to September (MJJAS) and November to March (NDJFM). The precipitation averaged for the five months over the monsoon area represents the global monsoon intensity (Zhou et al., 2008).

410

There is little difference in land monsoon regions between the *piControl* and *midHolocene* (Fig. 8b), but still an increased area globally by 9 % in the *midHolocene* with the majority of this increase (85 %) located in the SH (Fig. 8b and Fig. 9a). The greatest difference is found in the Southern Indian Ocean where South African and Australian monsoon regions meet (Fig. S5). However, the SH monsoon intensity decreases in the same period

415 (Fig. 9b) and the expansion in this monsoon region is not linked to any visible change in summer temperature or

sea level pressure (Fig. S6a and Fig. S6b). It is likely caused by the precipitation decrease over the eastern Indian Ocean during the SH winter being larger than the decrease during the SH summer, leading to stronger seasonal differences (Fig. S5a and Fig. S5b).
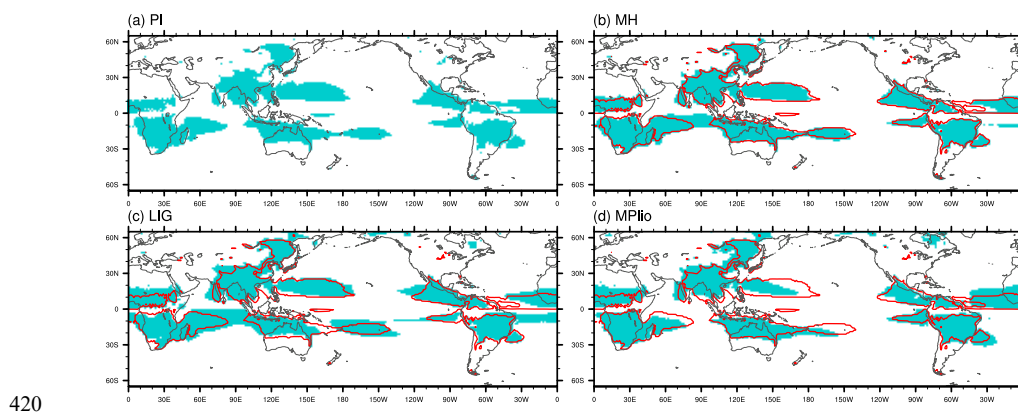
Figure 8. Global monsoon area in (a) the *piControl*, (b) the *midHolocene*, (c) the *lig127k*, (d) the *midPliocene* simulation, with *piControl* global monsoon boundary as red line in b-d.
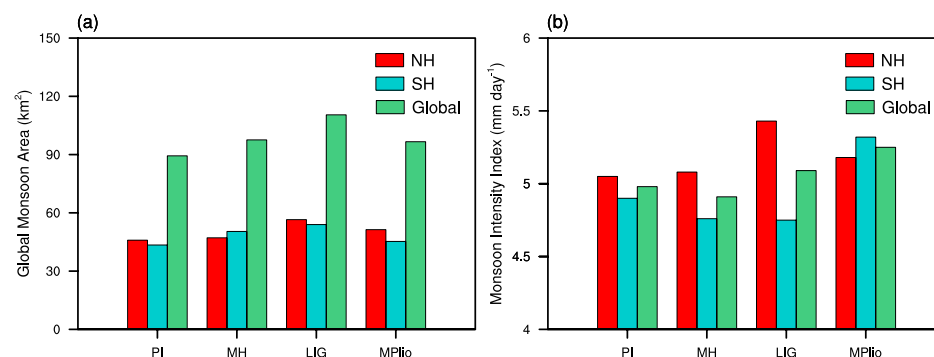
Figure 9. Global monsoon area (a) and Monsoon intensity (b) for global, the NH and the SH in the four simulations.

The Last Interglacial experiences northward expansions of NH monsoon regions (northern Africa, Asia and northern America) compared to pre-industrial, while the expansions in the SH monsoon regions are mainly located over the ocean (Fig. 8c). Although the monsoon area increases in both hemispheres, the intensity has only increased in the NH and instead decreased in the SH (Fig. 9b). MJJAS exhibits positive temperature anomalies and negative pressure anomalies over land in *lig127k*, favour a strengthening of monsoons (Webster et al., 1998). NDJFM experiences a global decrease in temperature except the Arctic region, positive pressure anomalies over land and negative pressure anomalies over the ocean, leading to a weakening of the negative land-ocean pressure gradients often linked to monsoonal flows. This is consistent with the PMIP4-CMIP6 *lig127k* ensemble, showing

Geoscientific
Model Development
Discussions

that the insolation changes during the *lig127k* lead to an intensification of boreal summer monsoons in the NH and a weakening of the austral summer monsoons in the SH (Otto-Bliesner et al., 2020).

440   The global monsoon area increases with of 8 % during the *midPliocene*, which comes mainly from the NH (75 %), while the increase in monsoon intensity mainly comes from the SH (9 % in the SH compared to 3 % in the NH) (Fig. 9). Compared to the other two interglacial periods, *midPliocene* is the only period which has a higher monsoon intensity in the SH than in the NH. All NH monsoon regions except North America experience a northward expansion in MJJAS (Fig. 8d), consistent with strengthened latitudinal and land-sea temperature

445   contrast and deepening of the low-pressure areas over Eurasia, North Africa and the North Atlantic (Fig. S5g). It is also consistent with the northward expansion of Hadley circulation (Fig. 5e). The precipitation intensity increase found in SH monsoon regions (NDJFM) is not linked to any strengthened land-sea pressure gradients (Fig. S5h). It might be the result of both a slightly strengthened land-sea thermal gradient for South America and southern Africa and a general temperature increase leading to higher specific humidity and increased moisture transport to

450   the monsoon regions.

### 4.6   Reponses in the modes of climate variability

Lastly, we examine the simulated climate variability modes on interannual and longer timescales associated with changes in sea surface temperature patterns, namely, the El Niño-Southern Oscillation (ENSO), the Pacific Decadal Oscillation (PDO) and the Atlantic Multidecadal Oscillation (AMO). We define the interannual

455   variability of monthly SST anomalies in the tropical Pacific basin as ENSO spatial pattern, and the leading EOF1 time series as ENSO index. The PDO is calculated by the leading EOF of monthly SST anomalies in the North Pacific and PC1 time series following (Mantua and Hare, 2002). Similarly, the AMO is estimated by the leading EOF of monthly SST anomalies in the North Atlantic (Guan and Nigam, 2009).

The simulations show a decline of ENSO intensity from the *piControl* to the *midHolocene*, the *lig127k* and the

460   *midPliocene*, which is universal across the equatorial central/eastern Pacific (Fig. 10). The Atlantic Niño variability is consistently weakened. The reduced ENSO variability during the Mid-Holocene is consistent with previous studies, either from proxy reconstructions (see a synthesis in Emile-Geay et al. (2016)) or model simulations (see a review by Lu et al. (2018)). The larger insolation anomalies in the *lig127k* compared to the *midHolocene* (Fig. 1) contribute to the more robust weakening of ENSO variability through reduced Bjerknes

465   feedbacks (Liu et al., 2014; Lu et al., 2019).
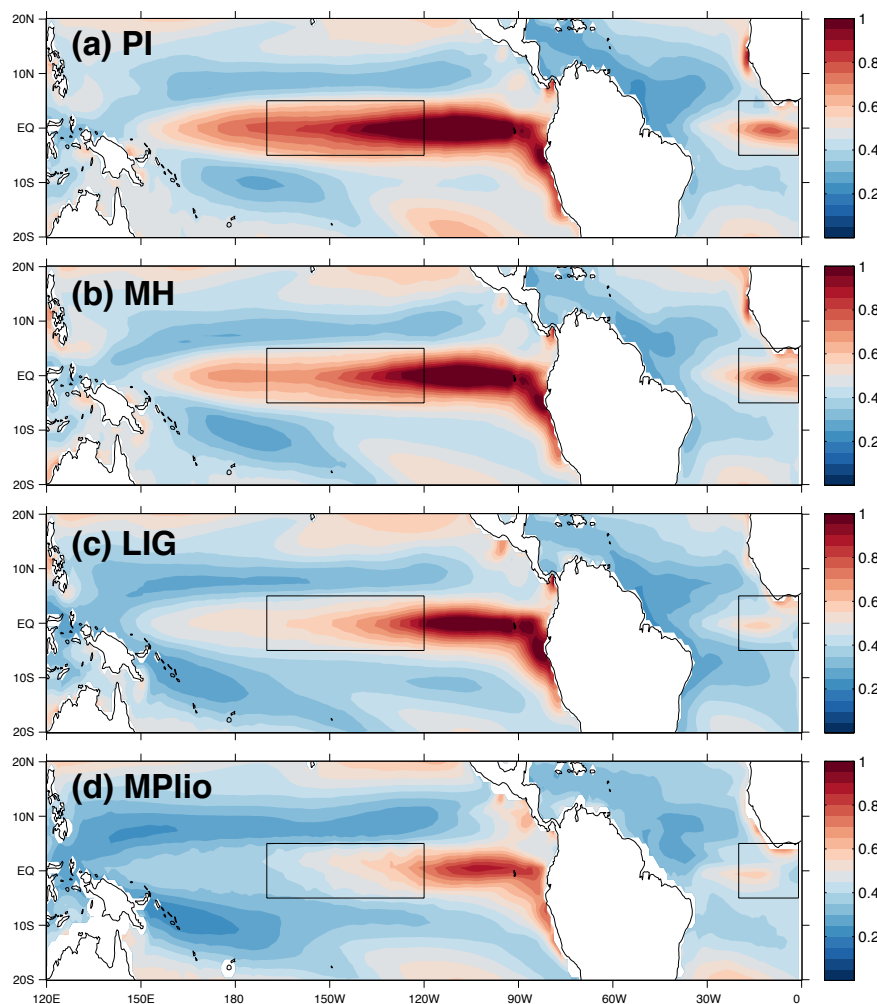
Figure 10. Simulated SST interannual variability (standard deviation of SST anomalies after removing seasonal cycle, unit: ℃) for all simulations. Black boxes are Niño 3.4 and Atlantic 3 regions (for the El Niño-Southern
470 Oscillation and Atlantic Niño, respectively).

The simulated PDO patterns generally reproduce the positive SST anomalies that are comparable in the equatorial eastern Pacific and in the Northeast Pacific and negative anomalies in the central and western North Pacific (Fig. 11). This internal PDO variability in paleoclimate conditions is consistent with a previous mid-Holocene study using earlier-generation climate models (An and Park, 2013). However, different simulations show remarkable
475 changes of the relative amplitude: in the *midHolocene* and *lig127k* the anomalies in the tropics are much larger and are almost equal to those in the Northeast Pacific. In the *midPliocene* the overall anomalies are weaker and stretch westward to the west coast of the tropical Pacific, which may contribute to the westward shift of Walker circulation (Fig. 5f).

19
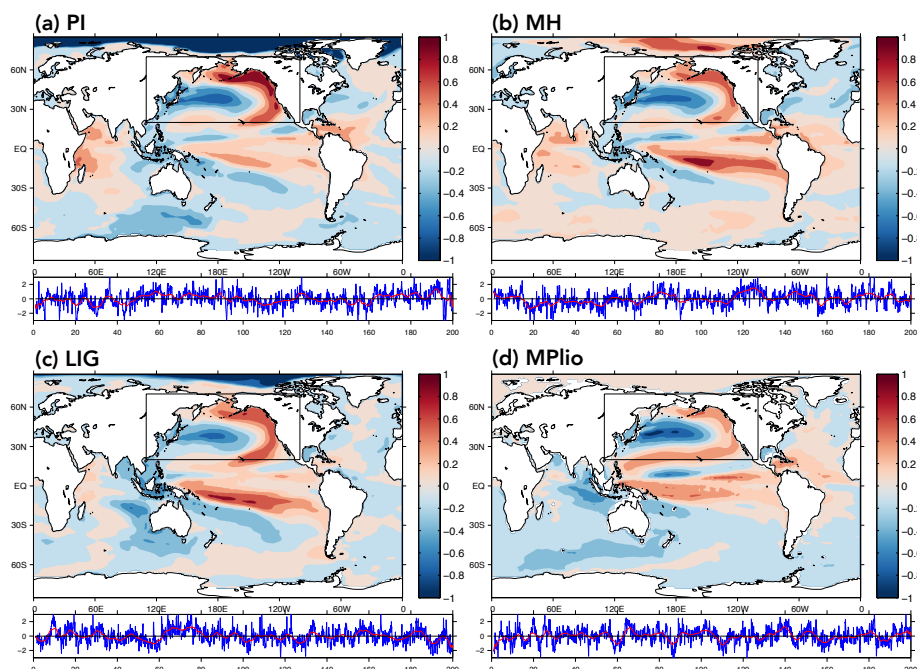
480 **Figure 11**. Simulated Pacific Decadal Oscillation (PDO) patterns. The spatial patterns show the leading empirical orthogonal function (EOF) of SST anomalies over the North Pacific (after removing the global mean SST anomaly). Note that the EOF calculation is restricted to the North Pacific (outlined by the black box). The global pattern is the regression coefficient of the monthly SST anomalies at each location onto the normalized principal component (PC) time series (unit: °C/°C). The time series show the associated PC time series (blue line) and the
485 10-year running mean (red line).

The AMO patterns in the EC-Earth3-LR simulations are characterized by a basin-wide mode in the North Atlantic (Fig. 12). The low-frequency mode has also been simulated in an earlier study during the Holocene (Wei and Lohmann, 2012). These anomalies also have a horseshoe shape (Gastineau and Frankignoul, 2015) with larger subpolar and subtropical anomalies. The spatial patterns of the AMO are largely unchanged in the *piControl*,
490 *lig127k* and *midPliocene* simulations but seems more predominant in the *midHolocene*.

The spectral feature of the simulated ENSO, PDO, and AMO are detected using the power spectrum method. The power spectra show that the dominant periodicities of ENSO, PDO and AMO lie in the 2-7 year, 8-20 year and 20- 40 year time scales (Fig. S7), all are statistically significant, although the spectral peak differs slightly. These periodicities are consistent with present-day observation (see a review by Deser et al. (2010)) and highlight the
495 model's capability to reproduce the representative natural internal variability.

Geoscientific
Model Development
Discussions
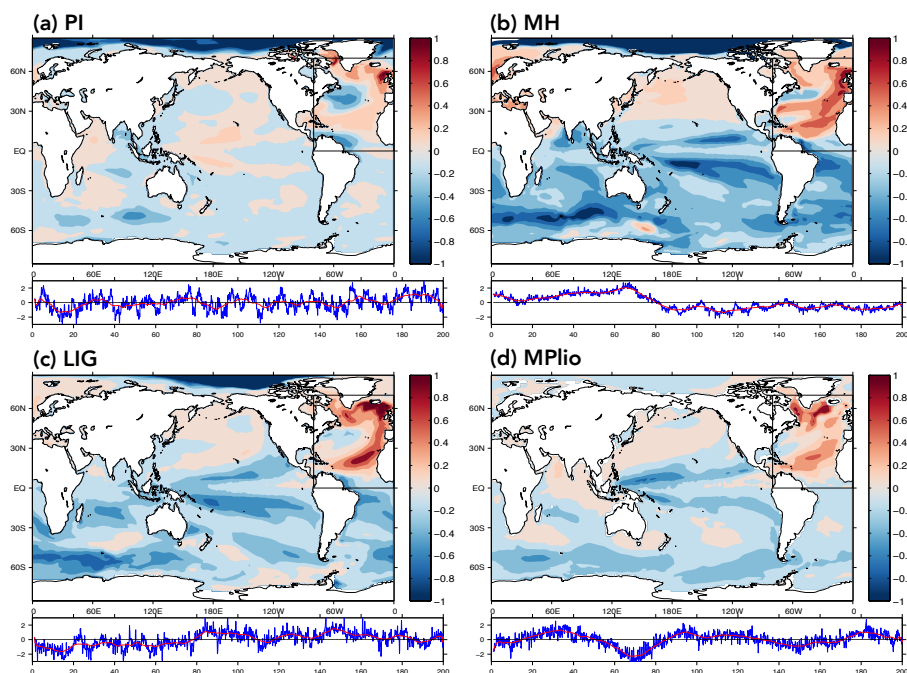
Figure 12. Simulated Atlantic Multidecadal Oscillation (AMO) patterns. The spatial patterns and time series are derived using the same EOF and regression method as PDO, but for the North Atlantic region (outlined by the black box).

5 Conclusion

This paper documents the four PMIP4-CMIP6 experiments performed by EC-Earth3-LR by providing the information on the model, experiments setup and results on large scale climate responses. The model outputs from the four simulations are published on ESGF for more applications by the research community. We expect that these data will be further used in studies through model-data comparison to understand the past climate change and climate variability, model-model and model-data comparison to improve the climate model performance, or multi-periods comparison to obtain an overview of the climate history.

We have followed PMIP4 protocol and adapted the climate forcing and boundary conditions in the EC-Earth3-LR. For the two interglacial simulations, most of the boundary conditions are prescribed as the same as the pre-industrial conditions. The boundary conditions such as vegetations, aerosols, dust forcings, are very important to sensitivity studies and should be properly prescribed during these climate conditions in the future simulations. We try to perform the spin-up runs as long as possible, but due to limited computation resources and time constrains, the deep ocean may not be in fully equilibrium in some of the simulations. The surface parameters have reached an acceptable equilibrium states as required by PMIP4.

The EC-Earth3-LR simulates reasonable climate response during past warm periods as shown in the other PMIP4-CMIP6 model ensemble. These warm periods are caused by the different forcings: the two interglacial simulations are forced by the insolation change and the mid-Pliocene simulation is forced by the high CO_2 concentration

520　comparable to today. The results show that the climate response in the latter forcing is dramatically greater than the former ones, implying the ongoing global warming is critical in the context of long climate history.

Climate changes are amplified over the land in the higher latitudes, especially in the Arctic region. Arctic warming is apparent in all simulations with a strong link between the seasonal cycles of surface air temperature and sea ice,

525　as well as a strong link between the surface air temperature and insolation anomalies in the *midHolocene* and *lig127k* simulations. The climatic response in the Antarctic region is less prominent, and only small changes are observed in the two interglacial simulations.

The changes in temperature gradient leads to a poleward expansion of Hadley circulation in all three warm period

530　simulations, with a reduced intensity in the Northern Hemisphere. In the southern hemisphere, the Hadley circulation strengthened in the *midHolocene* and *lig127k* but reduced in the *midPliocene*. We also found a strengthening and westward shift of the Pacific Walker circulation in all the three the three periods which is related to the changes in ENSO.

535　The global monsoon area increased in the *midHolocene* compared to the *piControl,* with the majority of the increase located in the SH. However, the SH monsoon intensity decreased due to stronger seasonal precipitation differences. In *lig127k,* the global monsoon area expanded northward and the monsoon intensity increased in the NH while it decreased in SH due to changes in the land-ocean thermal contrast in both hemispheres. For the *midPliocene*, both the global monsoon area and intensity increased, where the NH mainly contributed to the area

540　increase and the SH to the intensity increase.

The EC-Earth3-LR reproduces reasonable spatial patterns and frequency features of several intrinsic climate variability modes such as ENSO, PDO and AMO. ENSO variability is found to be weakened from pre-industrial towards *midHolocene*, *lig127k* and *midPliocene*, in response to intensified insolation changes in seasonality. The

545　changes in PDO and AMO are more subtle and complex and will need further investigation.

----

555   Details on the ESGF can be found on the website of the CMIP Panel (https://www.wcrp-climate.org/wgcm-cmip/wgcm-cmip6).

Supplement. The supplement related to this article is attached as *PMIP4-EC-Earth-supplement.doc*.

References

570   An, S.-I., and Park, J.-H.: Maintenance of PDO variability during the mid-holocene in PMIP2, Climate dynamics, 40, 1291-1299, 2013.

Bayr, T., Dommenget, D., Martin, T., and Power, S. B.: The eastward shift of the Walker Circulation in response to global warming and its relationship to ENSO variability, Climate dynamics, 43, 2747-2763, 2014.

Berger, A.: Long-term variations of daily insolation and Quaternary climatic changes, Journal of the atmospheric sciences, 35,
575   2362-2367, 1978.

Brierley, C. M., Zhao, A., Harrison, S. P., Braconnot, P., Williams, C. J. R., Thornalley, D. J. R., Shi, X., Peterschmitt, J. Y., Ohgaito, R., Kaufman, D. S., Kageyama, M., Hargreaves, J. C., Erb, M. P., Emile-Geay, J., D'Agostino, R., Chandan, D., Carré, M., Bartlein, P., Zheng, W., Zhang, Z., Zhang, Q., Yang, H., Volodin, E. M., Tomas, R. A., Routson, C., Peltier, W. R., Otto-Bliesner, B., Morozova, P. A., McKay, N. P., Lohmann, G., Legrande, A. N., Guo, C., Cao, J., Brady, E., Annan, J. D.,
580   and Abe-Ouchi, A.: Large-scale features and evaluation of the PMIP4-CMIP6 midHolocene simulations, Clim. Past Discuss., 2020, 1-35, 10.5194/cp-2019-168, 2020.

Burls, N. J., and Fedorov, A. V.: Wetter subtropics in a warmer world: Contrasting past and future hydrological cycles, Proceedings of the National Academy of Sciences, 114, 12888-12893, 10.1073/pnas.1703421114, 2017.

Chapman, W. L., and Walsh, J. E.: Simulations of Arctic Temperature and Pressure by Global Coupled Models, Journal of
585   Climate, 20, 609-632, 10.1175/jcli4026.1, 2007.

Corvec, S., and Fletcher, C. G.: Changes to the tropical circulation in the mid-Pliocene and their implications for future climate, Clim. Past, 13, 135-147, 10.5194/cp-13-135-2017, 2017.

de Boer, B., Haywood, A. M., Dolan, A. M., Hunter, S. J., and Prescott, C. L.: The Transient Response of Ice Volume to Orbital Forcing During the Warm Late Pliocene, Geophysical Research Letters, 44, 10,486-410,494, 10.1002/2017gl073535,
590   2017.

de Nooijer, W., Zhang, Q., Li, Q., Zhang, Q., Li, X., Zhang, Z., Guo, C., Nisancioglu, K. H., Haywood, A. M., Tindall, J. C., Hunter, S. J., Dowsett, H. J., Stepanek, C., Lohmann, G., Otto-Bliesner, B. L., Feng, R., Sohl, L. E., Tan, N., Contoux, C., Ramstein, G., Baatsen, M. L. J., von der Heydt, A. S., Chandan, D., Peltier, W. R., Abe-Ouchi, A., Chan, W. L., Kamae, Y., and Brierley, C. M.: Evaluation of Arctic warming in mid-Pliocene climate simulations, Clim. Past Discuss., 2020, 1-30,
595   10.5194/cp-2020-64, 2020.

Deser, C., Alexander, M. A., Xie, S.-P., and Phillips, A. S.: Sea Surface Temperature Variability: Patterns and Mechanisms, Annual Review of Marine Science, 2, 115-143, 10.1146/annurev-marine-120408-151453, 2010.

Dowsett, H., Dolan, A., Rowley, D., Moucha, R., Forte, A. M., Mitrovica, J. X., Pound, M., Salzmann, U., Robinson, M., Chandler, M., Foley, K., and Haywood, A.: The PRISM4 (mid-Piacenzian) paleoenvironmental reconstruction, Clim. Past, 600 12, 1519-1538, 10.5194/cp-12-1519-2016, 2016.

Döscher et al., The EC-Earth3 Earth System Model for the Climate Model Intercomparison Project 6. To be submiited to GMD, 2020.

Emile-Geay, J., Cobb, K. M., Carré, M., Braconnot, P., Leloup, J., Zhou, Y., Harrison, S. P., Corrège, T., McGregor, H. V., Collins, M., Driscoll, R., Elliot, M., Schneider, B., and Tudhope, A.: Links between tropical Pacific seasonal, interannual and 605 orbital variability during the Holocene, Nature Geoscience, 9, 168-173, 10.1038/ngeo2608, 2016.

Eyring, V., Bony, S., Meehl, G. A., Senior, C. A., Stevens, B., Stouffer, R. J., and Taylor, K. E.: Overview of the Coupled Model Intercomparison Project Phase 6 (CMIP6) experimental design and organization, Geosci. Model Dev., 9, 1937-1958, 10.5194/gmd-9-1937-2016, 2016.

Feng, R., Otto-Bliesner, B. L., Xu, Y., Brady, E., Fletcher, T., and Ballantyne, A.: Contributions of aerosol-cloud interactions 610 to mid-Piacenzian seasonally sea ice-free Arctic Ocean, Geophysical Research Letters, 46, 9920-9929, 10.1029/2019gl083960, 2019.

Gastineau, G., and Frankignoul, C.: Influence of the North Atlantic SST Variability on the Atmospheric Circulation during the Twentieth Century, Journal of Climate, 28, 1396-1416, 10.1175/jcli-d-14-00424.1, 2015.

Guan, B., and Nigam, S.: Analysis of Atlantic SST Variability Factoring Interbasin Links and the Secular Trend: Clarified 615 Structure of the Atlantic Multidecadal Oscillation, Journal of Climate, 22, 4228-4240, 10.1175/2009jcli2921.1, 2009.

Harrison, S. P., and Prentice, C. I.: Climate and CO_2 controls on global vegetation distribution at the last glacial maximum: analysis based on palaeovegetation data, biome modelling and palaeoclimate simulations, Global Change Biology, 9, 983-1004, 2003.

Haywood, A. M., Dowsett, H. J., Dolan, A. M., Rowley, D., Abe-Ouchi, A., Otto-Bliesner, B., Chandler, M. A., Hunter, S. J., 620 Lunt, D. J., Pound, M., and Salzmann, U.: The Pliocene Model Intercomparison Project (PlioMIP) Phase 2: scientific objectives and experimental design, Clim. Past, 12, 663-675, 10.5194/cp-12-663-2016, 2016.

Haywood, A. M., Tindall, J. C., Dowsett, H. J., Dolan, A. M., Foley, K. M., Hunter, S. J., Hill, D. J., Chan, W. L., Abe-Ouchi, A., Stepanek, C., Lohmann, G., Chandan, D., Peltier, W. R., Tan, N., Contoux, C., Ramstein, G., Li, X., Zhang, Z., Guo, C., Nisancioglu, K. H., Zhang, Q., Li, Q., Kamae, Y., Chandler, M. A., Sohl, L. E., Otto-Bliesner, B. L., Feng, R., Brady, E. C., 625 von der Heydt, A. S., Baatsen, M. L. J., and Lunt, D. J.: A return to large-scale features of Pliocene climate: the Pliocene Model Intercomparison Project Phase 2, Clim. Past Discuss., 2020, 1-40, 10.5194/cp-2019-145, 2020.

Hazeleger, W., Severijns, C., Semmler, T., Ştefănescu, S., Yang, S., Wang, X., Wyser, K., Dutra, E., Baldasano, J. M., and Bintanja, R.: EC-Earth: a seamless earth-system prediction approach in action, Bulletin of the American Meteorological Society, 91, 1357-1363, 2010.

630 Hazeleger, W., Wang, X., Severijns, C., Ştefănescu, S., Bintanja, R., Sterl, A., Wyser, K., Semmler, T., Yang, S., and Van den Hurk, B.: EC-Earth V2. 2: description and validation of a new seamless earth system prediction model, Climate dynamics, 39, 2611-2629, 2012.

Helsen, M. M., van de Wal, R. S. W., Reerink, T. J., Bintanja, R., Madsen, M. S., Yang, S., Li, Q., and Zhang, Q.: On the importance of the albedo parameterization for the mass balance of the Greenland ice sheet in EC-Earth, The Cryosphere, 11, 635 1949-1965, 10.5194/tc-11-1949-2017, 2017.

Hind, A., Zhang, Q., and Brattström, G.: Problems encountered when defining Arctic amplification as a ratio, Scientific Reports, 6, 30469, 10.1038/srep30469, 2016.

Hobbs, W., Palmer, M. D., and Monselesan, D.: An Energy Conservation Analysis of Ocean Drift in the CMIP5 Global Coupled Models*, Journal of Climate, 29, 1639-1653, 10.1175/jcli-d-15-0477.1, 2016.

640 Jungclaus, J. H., Bard, E., Baroni, M., Braconnot, P., Cao, J., Chini, L. P., Egorova, T., Evans, M., González-Rouco, J. F., Goosse, H., Hurtt, G. C., Joos, F., Kaplan, J. O., Khodri, M., Klein Goldewijk, K., Krivova, N., LeGrande, A. N., Lorenz, S. J., Luterbacher, J., Man, W., Maycock, A. C., Meinshausen, M., Moberg, A., Muscheler, R., Nehrbass-Ahles, C., Otto-Bliesner, B. I., Phipps, S. J., Pongratz, J., Rozanov, E., Schmidt, G. A., Schmidt, H., Schmutz, W., Schurer, A., Shapiro, A. I., Sigl, M., Smerdon, J. E., Solanki, S. K., Timmreck, C., Toohey, M., Usoskin, I. G., Wagner, S., Wu, C. J., Yeo, K. L., 645 Zanchettin, D., Zhang, Q., and Zorita, E.: The PMIP4 contribution to CMIP6 – Part 3: The last millennium, scientific objective, and experimental design for the PMIP4 past1000 simulations, Geosci. Model Dev., 10, 4005-4033, 10.5194/gmd-10-4005-2017, 2017.

Kageyama, M., Albani, S., Braconnot, P., Harrison, S. P., Hopcroft, P. O., Ivanovic, R. F., Lambert, F., Marti, O., Peltier, W. R., Peterschmitt, J. Y., Roche, D. M., Tarasov, L., Zhang, X., Brady, E. C., Haywood, A. M., LeGrande, A. N., Lunt, D. J., 650 Mahowald, N. M., Mikolajewicz, U., Nisancioglu, K. H., Otto-Bliesner, B. L., Renssen, H., Tomas, R. A., Zhang, Q., Abe-Ouchi, A., Bartlein, P. J., Cao, J., Li, Q., Lohmann, G., Ohgaito, R., Shi, X., Volodin, E., Yoshida, K., Zhang, X., and Zheng, W.: The PMIP4 contribution to CMIP6 – Part 4: Scientific objectives and experimental design of the PMIP4-CMIP6 Last Glacial Maximum experiments and PMIP4 sensitivity experiments, Geosci. Model Dev., 10, 4035-4055, 10.5194/gmd-10-4035-2017, 2017.

655   Kageyama, M., Braconnot, P., Harrison, S. P., Haywood, A. M., Jungclaus, J. H., Otto-Bliesner, B. L., Peterschmitt, J. Y.,
      Abe-Ouchi, A., Albani, S., Bartlein, P. J., Brierley, C., Crucifix, M., Dolan, A., Fernandez-Donado, L., Fischer, H., Hopcroft,
      P. O., Ivanovic, R. F., Lambert, F., Lunt, D. J., Mahowald, N. M., Peltier, W. R., Phipps, S. J., Roche, D. M., Schmidt, G. A.,
      Tarasov, L., Valdes, P. J., Zhang, Q., and Zhou, T.: The PMIP4 contribution to CMIP6 – Part 1: Overview and over-arching
      analysis plan, Geosci. Model Dev., 11, 1033-1057, 10.5194/gmd-11-1033-2018, 2018.

660   Kageyama, M., Harrison, S. P., Kapsch, M. L., Löfverström, M., Lora, J. M., Mikolajewicz, U., Sherriff-Tadano, S., Vadsaria,
      T., Abe-Ouchi, A., Bouttes, N., Chandan, D., LeGrande, A. N., Lhardy, F., Lohmann, G., Morozova, P. A., Ohgaito, R., Peltier,
      W. R., Quiquet, A., Roche, D. M., Shi, X., Schmittner, A., Tierney, J. E., and Volodin, E.: The PMIP4-CMIP6 Last Glacial
      Maximum experiments: preliminary results and comparison with the PMIP3-CMIP5 simulations, Clim. Past Discuss., 2020,
      1-37, 10.5194/cp-2019-169, 2020.

665   Kamae, Y., Ueda, H., and Kitoh, A.: Hadley and Walker circulations in the mid-Pliocene warm period simulated by an
      atmospheric general circulation model, Journal of the Meteorological Society of Japan. Ser. II, 89, 475-493, 2011.

      Koenigk, T., Brodeau, L., Graversen, R. G., Karlsson, J., Svensson, G., Tjernström, M., Willén, U., and Wyser, K.: Arctic
      climate change in 21st century CMIP5 simulations with EC-Earth, Climate Dynamics, 40, 2719-2743, 2013.

      Liu, J., Wang, B., Ding, Q., Kuang, X., Soon, W., and Zorita, E.: Centennial Variations of the Global Monsoon Precipitation
670   in the Last Millennium: Results from ECHO-G Model, Journal of Climate, 22, 2356-2371, 10.1175/2008jcli2353.1, 2009.

      Liu, Z., Lu, Z., Wen, X., Otto-Bliesner, B. L., Timmermann, A., and Cobb, K. M.: Evolution and forcing mechanisms of El
      Niño over the past 21,000 years, Nature, 515, 550-553, 10.1038/nature13963, 2014.

      Lu, Z., Liu, Z., Zhu, J., and Cobb, K. M.: A Review of Paleo El Niño-Southern Oscillation, Atmosphere, 9, 130, 2018.

      Lu, Z., Liu, Z., Chen, G., and Guan, J.: Prominent Precession Band Variance in ENSO Intensity Over the Last 300,000 Years,
675   Geophysical Research Letters, 46, 9786-9795, 10.1029/2019GL083410, 2019.

      Mantua, N. J., and Hare, S. R.: The Pacific Decadal Oscillation, Journal of Oceanography, 58, 35-44,
      10.1023/A:1015820616384, 2002.

      Masson-Delmotte, V., Schulz, M., Abe-Ouchi, A., Beer, J., Ganopolski, A., Rouco, J. G., Jansen, E., Lambeck, K.,
      Luterbacher, J., and Naish, T.: Information from Paleoclimate Archives In: Climate Change 2013: The Physical Science Basis
680   Contribution of Working Group I to the Fifth Assessment Report of the Intergovernmental Panel on Climate Change ed TF
      Stocker et al, Cambridge, United Kingdom and New York, NY, USA, 2013.

      Otto-Bliesner, B. L., Braconnot, P., Harrison, S. P., Lunt, D. J., Abe-Ouchi, A., Albani, S., Bartlein, P. J., Capron, E., Carlson,
      A. E., Dutton, A., Fischer, H., Goelzer, H., Govin, A., Haywood, A., Joos, F., LeGrande, A. N., Lipscomb, W. H., Lohmann,
      G., Mahowald, N., Nehrbass-Ahles, C., Pausata, F. S. R., Peterschmitt, J. Y., Phipps, S. J., Renssen, H., and Zhang, Q.: The
685   PMIP4 contribution to CMIP6 – Part 2: Two interglacials, scientific objective and experimental design for Holocene and Last
      Interglacial simulations, Geosci. Model Dev., 10, 3979-4003, 10.5194/gmd-10-3979-2017, 2017.

      Otto-Bliesner, B. L., Brady, E. C., Zhao, A., Brierley, C., Axford, Y., Capron, E., Govin, A., Hoffman, J., Isaacs, E.,
      Kageyama, M., Scussolini, P., Tzedakis, P. C., Williams, C., Wolff, E., Abe-Ouchi, A., Braconnot, P., Ramos Buarque, S.,
      Cao, J., de Vernal, A., Guarino, M. V., Guo, C., LeGrande, A. N., Lohmann, G., Meissner, K., Menviel, L., Nisancioglu, K.,
690   O'Ishi, R., Salas Y Melia, D., Shi, X., Sicard, M., Sime, L., Tomas, R., Volodin, E., Yeung, N., Zhang, Q., Zhang, Z., and
      Zheng, W.: Large-scale features of Last Interglacial climate: Results from evaluating the lig127k simulations for CMIP6-
      PMIP4, Clim. Past Discuss., 2020, 1-41, 10.5194/cp-2019-174, 2020.

      Peixoto, J. P., and Oort, A. H.: Physics of climate, 1992.

      Pithan, F., and Mauritsen, T.: Arctic amplification dominated by temperature feedbacks in contemporary climate models,
695   Nature Geoscience, 7, 181-184, 10.1038/ngeo2071, 2014.

      Salzmann, U., Haywood, A. M., Lunt, D. J., Valdes, P. J., and Hill, D. J.: A new global biome reconstruction and data-model
      comparison for the Middle Pliocene, Global Ecology and Biogeography, 17, 432-447, 10.1111/j.1466-8238.2008.00381.x,
      2008.

      Schulzweida, U.: CDO User Guide (Version 1.9. 6), Max Planck Institute for Meteorology: Hamburg, Germany, 2019.

700   Serreze, M., Barrett, A., Stroeve, J., Kindig, D., and Holland, M.: The emergence of surface-based Arctic amplification, The
      Cryosphere, 3, 11, 2009.

      Serreze, M. C., and Barry, R. G.: Processes and impacts of Arctic amplification: A research synthesis, Global and Planetary
      Change, 77, 85-96, 10.1016/j.gloplacha.2011.03.004, 2011.

      Stroeve, J., Holland, M. M., Meier, W., Scambos, T., and Serreze, M.: Arctic sea ice decline: Faster than forecast, Geophysical
705   Research Letters, 34, 10.1029/2007gl029703, 2007.

      Webster, P. J., Magaña, V. O., Palmer, T. N., Shukla, J., Tomas, R. A., Yanai, M., and Yasunari, T.: Monsoons: Processes,
      predictability, and the prospects for prediction, Journal of Geophysical Research: Oceans, 103, 14451-14510,
      10.1029/97jc02719, 1998.

710 Wei, W., and Lohmann, G.: Simulated Atlantic Multidecadal Oscillation during the Holocene, Journal of Climate, 25, 6989-7002, 10.1175/jcli-d-11-00667.1, 2012.

Yang, Z.-L., and Dickinson, R. E.: Description of the Biosphere-Atmosphere Transfer Scheme (BATS) for the Soil Moisture Workshop and evaluation of its performance, Global and Planetary Change, 13, 117-134, 10.1016/0921-8181(95)00041-0, 1996.

715 Yoshimori, M., and Suzuki, M.: The relevance of mid-Holocene Arctic warming to the future, Clim. Past, 15, 1375-1394, 10.5194/cp-15-1375-2019, 2019.

Zheng, J., Zhang, Q., Li, Q., Zhang, Q., and Cai, M.: Contribution of sea ice albedo and insulation effects to Arctic amplification in the EC-Earth Pliocene simulation, Clim. Past, 15, 291-305, 10.5194/cp-15-291-2019, 2019.

Zhou, T., Zhang, L., and Li, H.: Changes in global land monsoon area and total rainfall accumulation over the last half century, Geophysical Research Letters, 35, 10.1029/2008gl034881, 2008.

720